

K-Ion Batteries

Ultrarapid Nanomanufacturing of High-Quality Bimetallic Anode Library toward Stable Potassium-Ion Storage

Shuming Dou, Jie Xu, Danfeng Zhang, Wen Liu, Cuihua Zeng, Jiangchao Zhang, Zhedong Liu, Haoqiang Wang, Yani Liu, Yu Wang, Yanbing He, Wei-Di Liu, Wei Gan,* Yanan Chen,* and Qunhui Yuan*

Abstract: Bimetallic alloy nanomaterials are promising anode materials for potassium-ion batteries (KIBs) due to their high electrochemical performance. The most well-adopted fabrication method for bimetallic alloy nanomaterials is tube furnace annealing (TFA) synthesis, which can hardly satisfy the trade-off among granularity, dispersity and grain coarsening due to mutual constraints. Herein, we report a facile, scalable and ultrafast high-temperature radiation (HTR) method for the fabrication of a library of ultrafine bimetallic alloys with narrow size distribution ($\approx 10\text{--}20$ nm), uniform dispersion and high loading. The metal-anchor containing heteroatoms (i.e., O and N), ultrarapid heating/cooling rate ($\approx 10^3$ K s $^{-1}$) and super-short heating duration (several seconds) synergistically contribute to the successful synthesis of small-sized alloy anodes. As a proof-of-concept demonstration, the as-prepared BiSb-HTR anode shows ultrahigh stability indicated by negligible degradation after 800 cycles. The in situ X-ray diffraction reveals the K $^+$ storage mechanism of BiSb-HTR. This study can shed light on the new, rapid and scalable nanomanufacturing of high-quality bimetallic alloys toward extended applications of energy storage, energy conversion and electrocatalysis.

Introduction

The emerging potassium-ion batteries (KIBs), as one of the most promising alternatives for lithium-ion batteries (LIBs) in large-scale electrochemical energy storage systems (EESs), are attracting worldwide research interest. KIBs have the advantages of low cost, high element abundance (1.5 wt % for K vs. 0.0017 wt % for Li), and suitable redox potential (-2.93 V for K $^+$ /K vs. -3.04 V for Li $^+$ /Li, standard hydrogen electrode, SHE).^[1] The main obstacle to the extensive application of KIBs is that the repeated insertion/extraction of K ions with a large ionic radius (1.38 Å) induces serious volume expansion and even structural collapse of electrode materials, resulting in poor cycling performance.^[2] Therefore, it is urgent and crucial to develop

high-performance anode materials with highly reversible capacities and excellent cycling stabilities for advanced KIBs.

Alloying-type anode materials, such as Sb, Sn and Bi, possess significantly high specific capacities and suitable working voltage platforms,^[3] are known as promising candidates. However, the rapid capacity attenuations of alloying-type anodes caused by inherent volume expansions restrict their applications.^[4] To mitigate volume expansion, bimetallic alloying-type anodes composed of two metallic elements, capable of delivering electrochemical performance and stability, have attracted ever-increasing research interest.^[1,5] For instance, bimetallic Sb-based nanoparticles alloyed with Bi, Sn, Co, or Ni have demonstrated better

[*] S. Dou, H. Wang, Y. Liu, Y. Wang, Q. Yuan
 Shenzhen Key Laboratory of Flexible Printed Electronics Technology and School of Materials Science and Engineering, Harbin Institute of Technology (Shenzhen)
 Shenzhen 518055 (China)
 E-mail: yuanqunhui@hit.edu.cn

S. Dou, J. Xu, C. Zeng, J. Zhang, Z. Liu, Y. Chen
 School of Materials Science and Engineering, Key Laboratory of Advanced Ceramics and Machining Technology of Ministry of Education, Tianjin Key Laboratory of Composite and Functional Materials, Tianjin University
 Tianjin 300072 (China)
 E-mail: yananchen@tju.edu.cn

W. Gan
 Shenzhen Key Laboratory of Flexible Printed Electronics Technology and School of Science, Harbin Institute of Technology (Shenzhen)
 Shenzhen 518055 (China)
 E-mail: ganwei@hit.edu.cn

J. Xu
 State Key Laboratory of Mechanical Transmission, College of Materials Science and Engineering, Chongqing University
 Chongqing 400044 (China)

D. Zhang, W. Liu, Y. He
 Tsinghua Shenzhen International Graduate School,
 Tsinghua University
 Shenzhen 518055 (China)

W.-D. Liu
 Australian Institute of Bioengineering and Nanotechnology,
 The University of Queensland
 St. Lucia, Brisbane, Queensland, 4072 (Australia)

stress buffering capacities compared with pure Sb in K-alloying/dealloying.^[6]

Although several bimetallic alloying-type anodes have been investigated, little attention has been paid to how the nanostructures harness the performance of these anodes.^[7] This can be mainly attributed to the hardness of accurate structure control (such as coarsening/growth/agglomeration, nonuniform size distribution and volatilization of constituent metals) of such alloys during the conventional tube furnace annealing (TFA) treatment process due to the intrinsic slow heating/cooling rate ($<10\text{ Ks}^{-1}$) and long heating duration (several hours).^[8] Therefore, the manufacturing of ultrafine bimetallic alloy nanoparticles with high uniformity through a more facile and controllable method is an urgent need.

Recently, an electrical Joule-heating-based thermal shock synthesis method was proposed.^[9] In this process, due to the ultrahigh ramping/cooling rate ($10^3\text{--}10^5\text{ Ks}^{-1}$) and short heating duration (several seconds), ultrafast fabrication of ultrafine metallic nanoparticles on carbon nanofibers/films with relatively low metal contents have been realized.^[10] However, the scale-up manufacturing of well-dispersed metallic nanoparticles on carbon at high mass load via thermal shock synthesis has not been realized due to the limited carrying capacities of carbon nanofibers/films bearing small specific surface areas for metal precursors.

Herein, we report a facile, scalable and ultrafast high-temperature thermal radiation (HTR) synthesis for a series of ultrafine bimetallic alloy nanoparticles with narrow size distributions and high loading for KIBs anodes (Figure 1A). During this process, adequate temperature ($>1300\text{ K}$) can be instantly generated (within $\approx 15\text{ s}$) owing to the rapid heating/quenching rates ($\approx 10^3\text{ Ks}^{-1}$) as illustrated in Figure 1B. To achieve distinctive high metal loadings, ammonium citrate ($\text{C}_6\text{H}_{17}\text{N}_3\text{O}_7$) and sodium chloride (NaCl) are employed as carbon-source/metal-anchor and template/poregen, respectively. The high temperature enables simultaneous carbonization of organic components and an in situ pyrolysis/carbothermal reduction of metal salts. The formed N/O co-doped mesoporous carbon nanosheets with large specific surface area ensures the formation and stabilization of bimetallic nanoparticles.^[11] Meanwhile, the short manufacturing time avoids the agglomeration/evaporation of metal contents and achieves ultrafine alloy nanoparticles with homogeneous dispersion. Compared with the traditional TFA approach, the HTR strategy shows unique advantages, such as facile synthetic process/conditions and homogeneous nanoparticle size/morphology (Figure 1C). As a proof-of-concept demonstration, the BiSb decorated carbon with alloy particles of $\approx 15\text{ nm}$ (BiSb-HTR, Figure 1D and F) is applied as anode material for KIBs, showing high storage capacity and excellent cycling stability

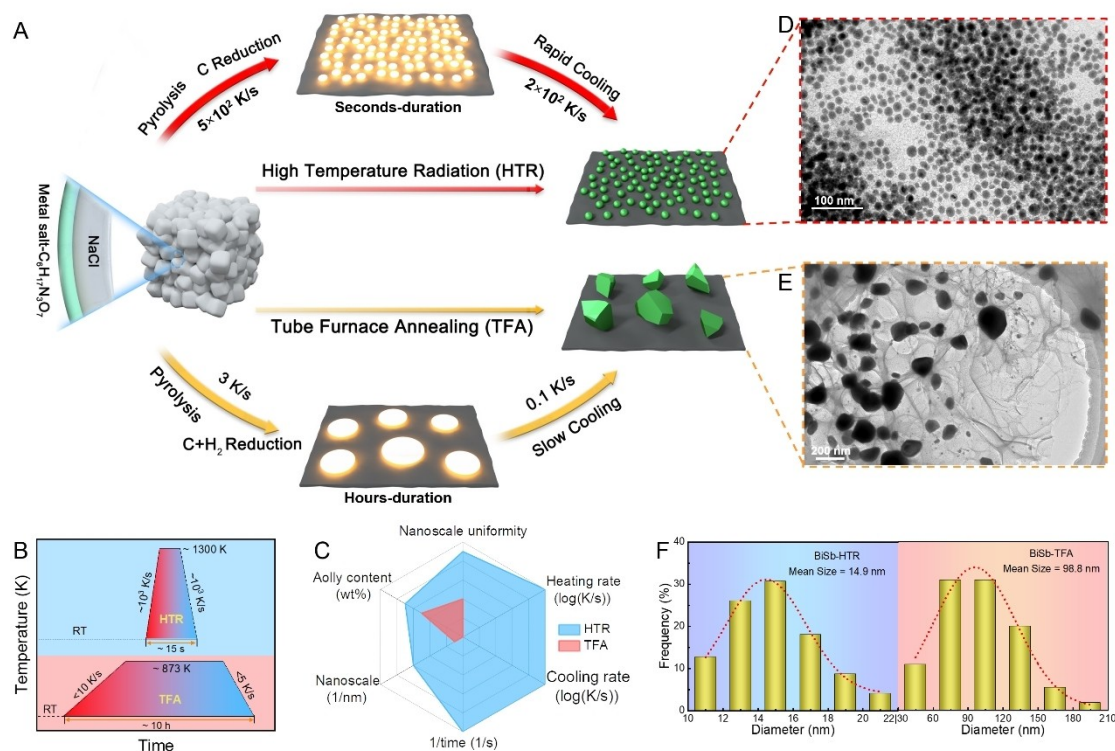


Figure 1. A) Schematic comparison between our HTR approach and conventional TFA method for the synthesis of bimetallic nanoparticles. B) Temperature profiles of the HTR and TFA processes. The whole HTR and TFA process takes $\approx 15\text{ s}$ and $\approx 10\text{ h}$, respectively. C) A radar plot showing a comparison between the conventional TFA method and our HTR approach in terms of reaction duration, heating/cooling rates, average size, alloy content, and nanoscale uniformity. The reaction duration is compared as the inverse of time. The higher value of the two methods is normalized to 1. D) TEM image of BiSb synthesized by HTR (BiSb-HTR). E) TEM image of BiSb synthesized by TFA (BiSb-TFA). F) Nanoparticle size distributions of BiSb-HTR and BiSb-TFA derived from the TEM images.

compared with its analogs obtained through the TFA synthesis (BiSb-TFA, Figure 1E and F). In addition, the formation mechanism of BiSb-HTR in the synthesis process is investigated by ex situ X-ray diffraction (XRD) together with SEM characterizations. Furthermore, in situ XRD technique reveals the K^+ storage mechanism of BiSb-HTR during the potassiation/depotassiation processes. This study can shed light on the new, rapid and scalable fabrication of high-quality bimetallic alloys toward extended applications of energy storage, energy conversion and electrocatalysis.

Results and Discussion

As shown in Figure S1, a homemade setup is used to carry out the HTR synthesis, during which an electrical pulse was applied to enable Joule heating to achieve precise control on the temperature and time of reaction. Taking BiSb-HTR as an example, the as-prepared white powdery precursors were spread on a carbon cloth (Figure 2A(i) and S2A). Figure 2A(ii) and the inset of Figure S2B show schematic diagrams and digital photographs of samples during HTR treatment, respectively. After the HTR treatment (Figure S2C), the precursor is converted into a carbon composite

containing bimetallic alloy nanoparticles and encapsulated NaCl, and the NaCl salts were subsequently removed by rinsing to get the final product (Figure 1D).

Ex situ XRD and SEM measurements were conducted to study the formation mechanism of the BiSb-HTR. Figure 2A shows ex situ contour plot of the XRD results obtained for the structural evaluation process of salt-loaded NaCl and the corresponding temperature-time evolution during the HTR treatment process. Initially, a typical HTR synthesis includes generating a high temperature of ≈ 1340 K in 3.0 s, holding constant temperature for 7.0 s and cooling down to room temperature in 5.0 s after turning off the power supply (Figure S2B). Before the HTR treatment, metal salt, $C_6H_{17}N_3O_7$ and NaCl are well-mixed and freeze-dried to obtain precursors. As illustrated in Figure 2B, the surface of the precursors is smooth. As the heating time is extended to 1.5 s, three peaks at 28.2° , 32.6° and 40.2° for precursor salts weaken or disappear (Figure 2A and S3), indicating that the decompositions of organic metal salts occur. Instead, when we increase the heating time from 1.5 s to 10.0 s, the four new peaks located at 27.8° , 38.7° , 40.6° and 49.9° , corresponding to the (012), (104), (110) and (202) crystal plane of BiSb-HTR, are gradually getting intensified, demonstrating that the ultrashort manufacturing time is

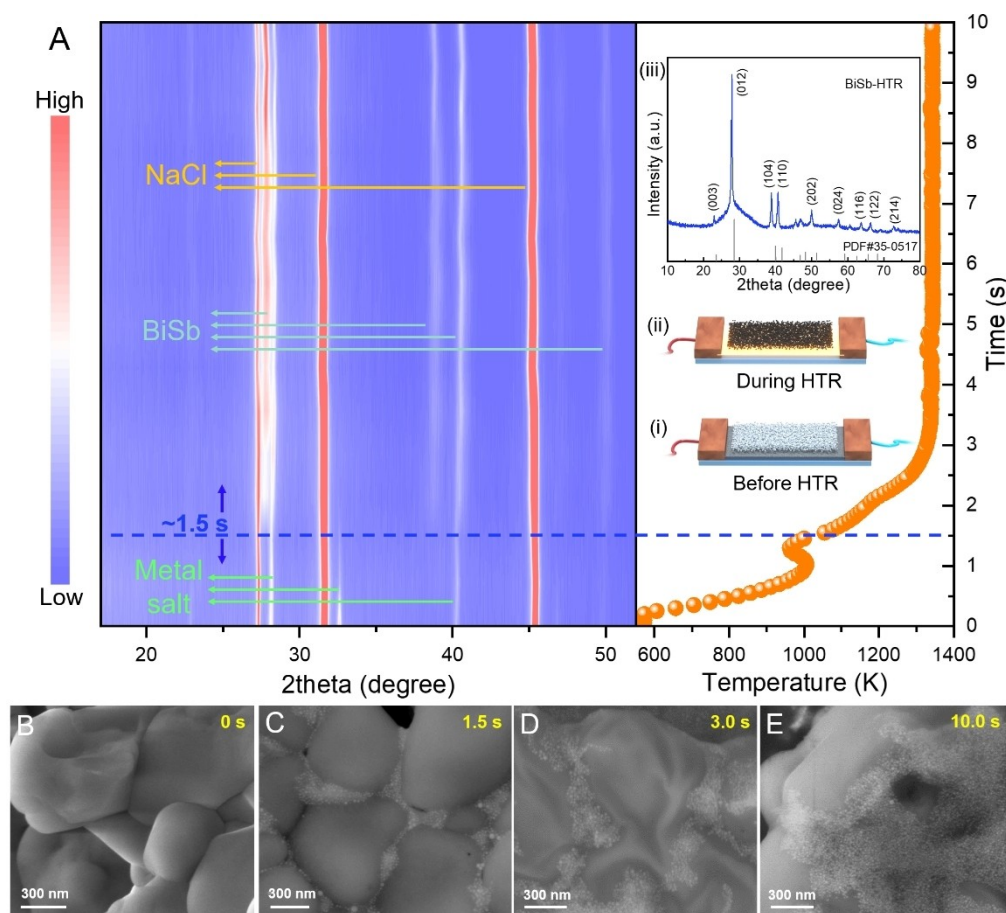


Figure 2. A) Ex situ contour plot of the XRD results representing the structural evaluation of precursors and the corresponding temperature-time evolution during an HTR treatment of ≈ 10 s. Inset i and ii are the schematic diagrams of samples before and during HTR treatment, respectively. Inset iii is the XRD pattern of BiSb-HTR. B)–E) SEM images of precursors upon heating under different times.

capable of achieving the ultrafast crystallization of the BiSb-HTR alloys. Meanwhile, as shown in Figure 2C, the ultrafine nanoparticles are firstly discovered between adjacent NaCl crystals. With a longer heating duration (≈ 3.0 s), the formation of crumpled carbon sheets and more alloy nanoparticles is observed (Figure 2D). The formed carbon sheets are beneficial for the formation and stabilization of bimetallic nanoparticles.^[11] The ultrarapid heating/cooling rate avoids the agglomeration/evaporation of metal contents and achieves ultrafine alloy nanoparticles with homogeneous dispersion. Upon prolonging the heating time to 10.0 s, thousands of ultrafine and homogeneous BiSb nanoparticle decorated carbon sheets are observed on the surface of NaCl crystals (Figure 2E). The XRD pattern of the BiSb-HTR in Figure 2A(iii) can be indexed to hexagonal BiSb alloy with the (166) space group (PDF#35-0517),^[12] proving the successful formation of the target composite through the HTR synthesis. Therefore, our ultrafast HTR synthesis method is more effective for fabricating ultrafine bimetallic alloy nanoparticles with narrow size distribution and uniform dispersion.

Morphology and size of the as-fabricated BiSb bimetallic nanoparticles are investigated by scanning electron microscopy (SEM) at low/high magnifications (Figure 3A and S4A), where the BiSb nanoparticles with an average particle size of 14.9 nm are uniformly embedded in the carbon

nanosheets. The transmission electron microscopy (TEM) image shown in Figure 3B further illustrates the nanoscale size and morphology features of BiSb-HTR. It is noteworthy that the BiSb nanoparticle shows a core-shell structure, with a crystallized core and an outer amorphous shell. In the high-resolution TEM (HRTEM) image in the inset of Figure 3B, the measured lattice fringes of 0.32 nm match well with the (012) crystal plane of BiSb. The diffraction rings in the selected area electron diffraction (SAED) pattern shown in Figure 3C further verifies the nanocrystalline structure of the ultrafine BiSb nanoparticles. The Bi and Sb elements are uniformly dispersed in the spherical BiSb nanoparticles, which are supported by the N-doped carbon substrate, as evidenced by high-angle annular dark-field scanning TEM (HAADF-STEM) and energy-dispersive spectroscopy (EDS) elemental mapping (Figure 3D and E).

For comparison, we use the same precursors to prepare the BiSb-TFA nanoparticles via the traditional TFA method with a heating rate (3 K s^{-1}) to 873 K, dwelled for 5 hours, followed by slowly cooling (0.1 K s^{-1}) to room temperature. The BiSb-TFA shows a similar XRD profile to BiSb-HTR without any other diffraction peaks for impurity phases (Figure S5A). Nevertheless, the BiSb-TFA nanoparticles present irregular polyhedral morphologies with a much wider size distribution from 30 nm to 210 nm (Figure S4B

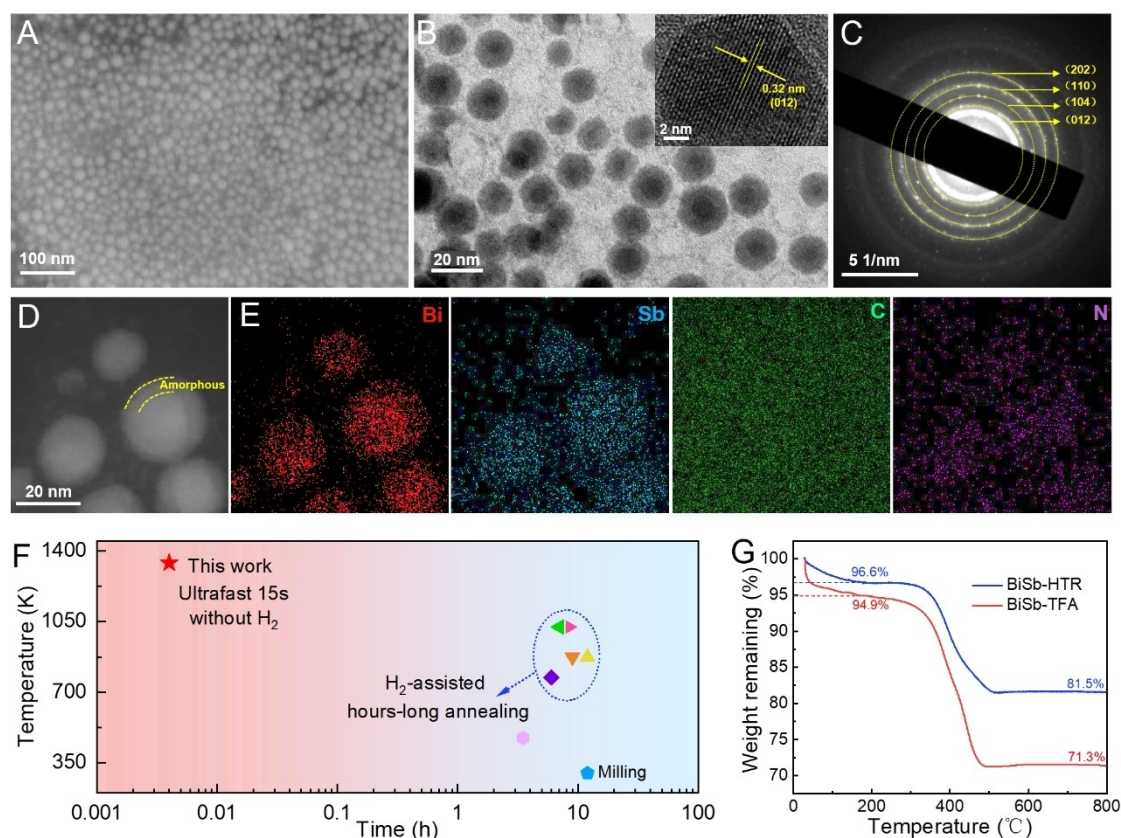


Figure 3. A) SEM image, B) high magnification TEM image, (inset) HRTEM image, C) SAED pattern, D) HAADF-STEM image, E) EDX-elemental mapping images of BiSb-HTR. F) Comparison of the heating temperature and time between this work and reported literatures. G) TGA curves of BiSb-HTR and BiSb-TFA.

and S5B–E) due to the slow heating/cooling rate and long annealing durations. As demonstrated in Figure 3F and Table S1,^[5,12,13] the fabrication technique used in this study can accomplish the preparation of high-quality bimetallic alloys in an ultrashort duration of ≈ 15 s at a high temperature of ≈ 1340 K, which can effectively avoid the evaporation of metallic components, the risky utilization of H_2 , and eventually leading to a nanostructure with uniformly dispersed ultrafine alloys at high mass loading. Additionally, such high efficiency is extremely beneficial for the scale-up manufacturing of these materials. To demonstrate the superiority of the fast preparation for synthesizing bimetallic alloy nanoparticles, the contents of alloy constituents are evaluated through thermogravimetric analysis (TGA). The alloy content of the BiSb-TFA is calculated to be $\approx 65.6\%$, whereas the BiSb-HTR has a higher alloy content of $\approx 73.7\%$ (Figure 3G).

The nitrogen adsorption/desorption isotherm was carried out to evaluate the porosity characteristics of BiSb-HTR, as shown in Figure S6A and S6B. It can be seen that the BiSb-HTR has a typical type IV adsorption/desorption curve with H1 type hysteresis loop, demonstrating its mesoporous structure. In addition, the BiSb-HTR possesses a specific surface area of $214.4\text{ m}^2\text{ g}^{-1}$, accompanied by a dominating pore diameter of 39.1 nm. Such mesoporous architecture can contribute to the fast diffusion of K ions, leading to outstanding cycling stability. The BiSb-TFA has a mesoporous structure similar to BiSb-HTR (Figure S6C and S6D). The two peaks located at 1322 and 1582 cm^{-1} in Raman spectrums (Figure S7A) can be assigned to the disordered D-band and graphitic G-band, respectively.^[14] The similar I_D/I_G ratios of BiSb-HTR and BiSb-TFA indicate the typical amorphous carbon structure in the nanomaterials. The X-ray photoelectron spectroscopy (XPS) analysis is employed to investigate the chemical composition of the BiSb-HTR nanoparticles, where Bi, Sb, C, N and O elements have been observed (Figure S7B). Attentively, the appearance of O/N should be originated from the carbonization of organic components and ammonium citrate. In addition, the XPS spectrum of Bi 4f (Figure S7C) is separated into two peaks centered at 159.7 and 165.0 eV, corresponding to Bi $4f_{7/2}$ and Bi $4f_{5/2}$, respectively. The two peaks with bonding energies of 531.0 and 540.4 eV in the Sb 3d spectrum correspond to Sb $3d_{5/2}$ and Sb $3d_{3/2}$, respectively (Figure S7D). Due to the surface oxidation of the sample during the test process, the binding energies of Bi $4f_{7/2}$ and Sb $3d_{5/2}$ are higher than the standard Bi⁰ $4f_{7/2}$ and Sb⁰ $3d_{5/2}$ values, as confirmed by the abnormal signal O 1s in Figure S7D. This phenomenon is similar to the reported results in the literatures.^[3b,15] The carbon bonding was analyzed by fitting the high-resolution XPS spectrum of C 1s (Figure S7E) as four peaks located at 284.6, 285.6, 288.1 and 292.2 eV, corresponding to the C–C/C=C, C–O/C–N, C=O and HO–C=O, respectively. The N 1s spectrum in Figure S7F deconvoluted into the three peaks reveals the presence of pyridinic nitrogen (N-6), pyrrolic nitrogen (N-5) and graphitic nitrogen (N–Q),^[16] demonstrating the successful doping of N heteroatom into the carbon matrix.^[17]

It is known that the composition of electrolyte has an important influence on the reactions at electrode/electrolyte interface and the cycling properties of electrodes.^[18] In this regard, the electrochemical performance of the as-fabricated BiSb-HTR was evaluated in three kinds of electrolytes including 0.8 M KPF₆ in EC/DEC, 3 M KFSI in DME and 5 M KFSI in DME. In a traditional ester-based electrolyte (0.8 M KPF₆ in EC/DEC), the discharge/charge capacities of BiSb-HTR anode demonstrate fast fading during 200 cycles at current densities of 0.2 and 0.5 A g^{-1} (Figure S8A and S8B), which is originated from the incompatibility of electrolyte components and alloy anodes, as well as the excessive decomposition of solvents.^[19] In contrast, when we changed the electrolyte from an ester-based KPF₆ electrolyte to an ether-based KFSI electrolyte (3 M KFSI in DME), the significantly enhanced cycling stability of BiSb-HTR anode was observed, delivering discharge specific capacities of 274.1 and 215.5 mAh g^{-1} after 200 cycles at current densities of 0.2 and 0.5 A g^{-1} (Figure S8C and S8D), respectively. These comparative results elucidate that the formation of stable SEI film in an ether-based KFSI electrolyte at a lower concentration can allow the alloy anode to achieve relatively stable cycles.^[19,20] In an ether-based KFSI electrolyte at 5 M, the BiSb-HTR anode presents the best performance, showing the maximum reversible capacities ($343.0/322.4\text{ mAh g}^{-1}$) at the 200th cycles at current densities of 0.2 and 0.5 A g^{-1} (Figure 4A). These comparative results signify that the different K⁺ solvation structures in the different electrolyte compositions may result in different electrochemical performances. The decreased solvent molecular polarization caused by the stronger interactions between FSI[−] and K⁺ can lead to higher electrolyte stability and compatibility with the alloy anode in the electrolyte of 5 M KFSI in DME, which accounts for the most remarkable potassium storage properties.^[21] Based on the above discussion, the optimized electrolyte composition (5 M KFSI in DME) was selected to test the electrochemical performance of BiSb-HTR electrodes in KIBs.

The initial three cyclic voltammetry (CV) curves of the BiSb-HTR anode are shown in Figure 4B. During the first discharge cycle, three broad cathodic peaks from 0.02 V to 1.25 V are observed, which can be ascribed to the generation of irreversible solid electrolyte interphase (SEI) layer on the surface of the electrode material, the irreversible intercalation of K ions in the carbon substrate, and the alloying reaction of K ions and BiSb nanoparticles. In the following discharging and charging processes, the appearance of two reduction peaks located at 0.61 and 0.20 V indicates the two-step alloying reaction: BiSb → KBiSb → K₃BiSb. Correspondingly, two oxidation peaks appearing at approximately 0.72 and 1.25 V indicate the reversible two-step depotassiation process of K₃BiSb → KBiSb → BiSb.^[13b] And the BiSb-TFA anode exhibits a similar dealloying/alloying reaction mechanism (Figure S9A). Notably, the CV curves of the BiSb-HTR anode are almost overlapped with each other after the first scan, manifesting the highly reversible potassiation/depotassiation behavior.

The galvanostatic charge–discharge (GCD) curves for BiSb-HTR are presented in Figure 4C at a current density

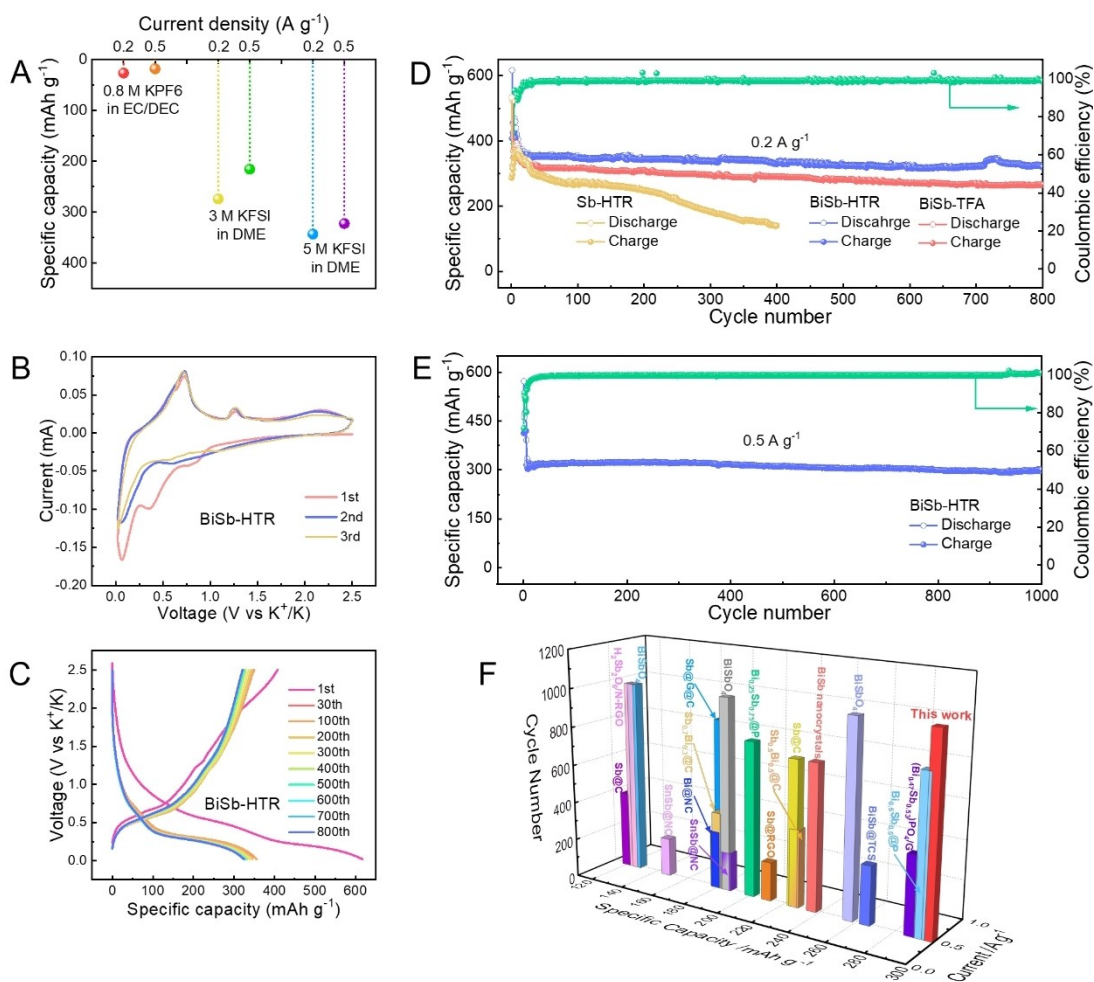


Figure 4. Electrochemical performance of samples as KIBs anodes in half cells: A) Specific capacities of BiSb-HTR using different electrolytes at the 200th cycle at 0.2 and 0.5 A g⁻¹. B) CV curves of BiSb-HTR at a scanning rate of 0.1 mV s⁻¹. C) GCD voltage plots of BiSb-HTR from the 1st to 800th cycles. D) Cycling performance of Sb-HTR, BiSb-HTR and BiSb-TFA at 0.2 A g⁻¹. E) Long-term cycling performance of BiSb-HTR at 0.5 A g⁻¹. F) Comparison in cycling performance of BiSb-HTR with other reported Bi/Sb-based KIBs anodes.

of 0.2 A g⁻¹. The BiSb-HTR anode can achieve an initial Coulombic efficiency (CE) of 66.1%, with discharge and charge capacities of 617.4 and 407.8 mA h g⁻¹. For the BiSb-TFA anode, a lower initial CE value of 62.4% is achieved, based on discharge and charge capacities of 524.7 and 327.4 mA h g⁻¹. The irreversible capacity loss in the first cycle can be related to the irreversible K⁺ insertion and the formation of SEI film. Most significantly, the GCD curves at the 30th, 100th, 200th, 300th, 400th, 500th, 600th, 700th and 800th cycles of the BiSb-HTR anode show no obvious difference, signifying the high cycling stability and electrochemical reversibility of the BiSb-HTR anode in KIBs. Figure 4D illustrates the superior cycling performance of BiSb-HTR anode over 800 cycles at 0.2 A g⁻¹. Interestingly, the stable CE over 98% for the BiSb-HTR anode is observed after 20 cycles in ether-based KFSI electrolyte, which has also been observed in previous studies.^[5,22] This phenomenon is mainly attributed to the relatively slow formation of SEI film in the ether-based electrolyte.^[19,21] Outstanding cycling stability is delivered with a high reversible capacity of

324.8 mA h g⁻¹ after 800 cycles, corresponding to a high capacity retention of 90.6% compared with the specific capacity value in the 30th cycle, along with an average capacity decay rate of 0.0088% per cycle. In contrast, the specific capacity of the Sb-HTR undergoes a fast fading, which is only 141.7 mA h g⁻¹ after 400 cycles with lower capacity retention (45.9%). The contrastive results indicate the bimetallic alloy nanoparticles (i.e., BiSb) have exceptional cycling stability compared with the monometallic nanoparticles (i.e., Sb), owing to the ameliorated stress buffering capability originating from the collaborative contribution of binary elements. As the cycle continues, the reversible specific capacity of BiSb-TFA gradually declines and delivers a capacity of 268.3 mA h g⁻¹ after 800 cycles (Figure 4D and S9B). These results suggest the ultrafine bimetallic alloys with narrow size distribution synthesized by the ultrafast HTR method can be given rise to the exceptional specific capacity of the BiSb-TFA anode. The rate performance of the BiSb-HTR is shown in Figure S9C, with discharge-specific capacities of 490.9, 356.9, 289.7, 222.2 and

114.3 mAhg⁻¹ at the current densities of 0.1, 0.2, 0.5, 1.0 and 2.0 Ag⁻¹. Notably, the BiSb-HTR electrode recovers a specific capacity of 350.0 mAhg⁻¹. For comparison, the BiSb-TFA anode shows lower specific capacities in rate testing (Figure S9D). Intriguingly, the BiSb-HTR can outperform the BiSb by the TFA approach in the terms of the rate properties and cycling stability in KIBs. Figure 4E shows the long-term cycling stability of the BiSb-HTR under a high current density of 0.5 Ag⁻¹. More impressively, as the cycling test advances, the reversible capacity of BiSb-HTR anode retains at 297.4 mAhg⁻¹ after 1000 cycles with a high capacity retention of ≈93.7%, accompanied by a low capacity decay rate of only 0.0063% per cycle comparing with the 10th cycle. By contrast, the BiSb-TFA anode shows a lower reversible capacity (229.1 mAhg⁻¹ after 1000 cycles) and a higher capacity decay rate, which are probably due to the relatively low alloy loading and large particles size of BiSb alloy in the BiSb-TFA nanocomposite (Figure S10A). The BiSb-HTR anode achieves reversible discharge capacities of 174.5 and 158.4 mAhg⁻¹ after 1000 and 2000 cycles at 1.0 Ag⁻¹ (Figure S10B). The electrochemical performance of BiSb-HTR is comparable or even better than those of other previously reported Bi/Sb-based KIBs anodes (Figure 4F).^[5,6,12,13b,c,22a,23] These results explicate that the unique

structural advantages of BiSb nanocomposite including ultrafine size, uniform distribution and high alloy content, are responsible for the ultrastable and highly reversible (de)potassiation storage behavior in KIBs.

To probe the K⁺ storage mechanism of BiSb-HTR as an anode in KIBs, in situ XRD technique was implemented and the contour plot results are illustrated in Figure 5. During the 1st K⁺ insertion process, the (012), (104) and (110) characteristic peaks of BiSb-HTR gradually weaken and eventually disappear. As discharging to 0.15 V, two new peaks with different intensities indexed to the (220) and (311) plane of K₃BiSb at 29.5° (strong) and 33.7° (weak) appear, elucidating the phase transfer from BiSb to K₃BiSb.^[13b] During the initial depotassiation, the characteristic peaks for intermediate phase (KBiSb) have arisen at 0.75 V, and finally turns to BiSb phase after further charging to 1.3 V. During the 2nd K⁺ intercalation round, two characteristic peaks of KBiSb are firstly observed at 0.6 V, and then replaced by the peaks of K₃BiSb due to the continuous potassiation,^[5] which is distinct from the structural evolution during the 1st potassiation. From the 2nd cycle, the subsequent charging process follows the same phase transformation as that in the 1st charging cycle although the discharging processes in the 1st and 2nd rounds

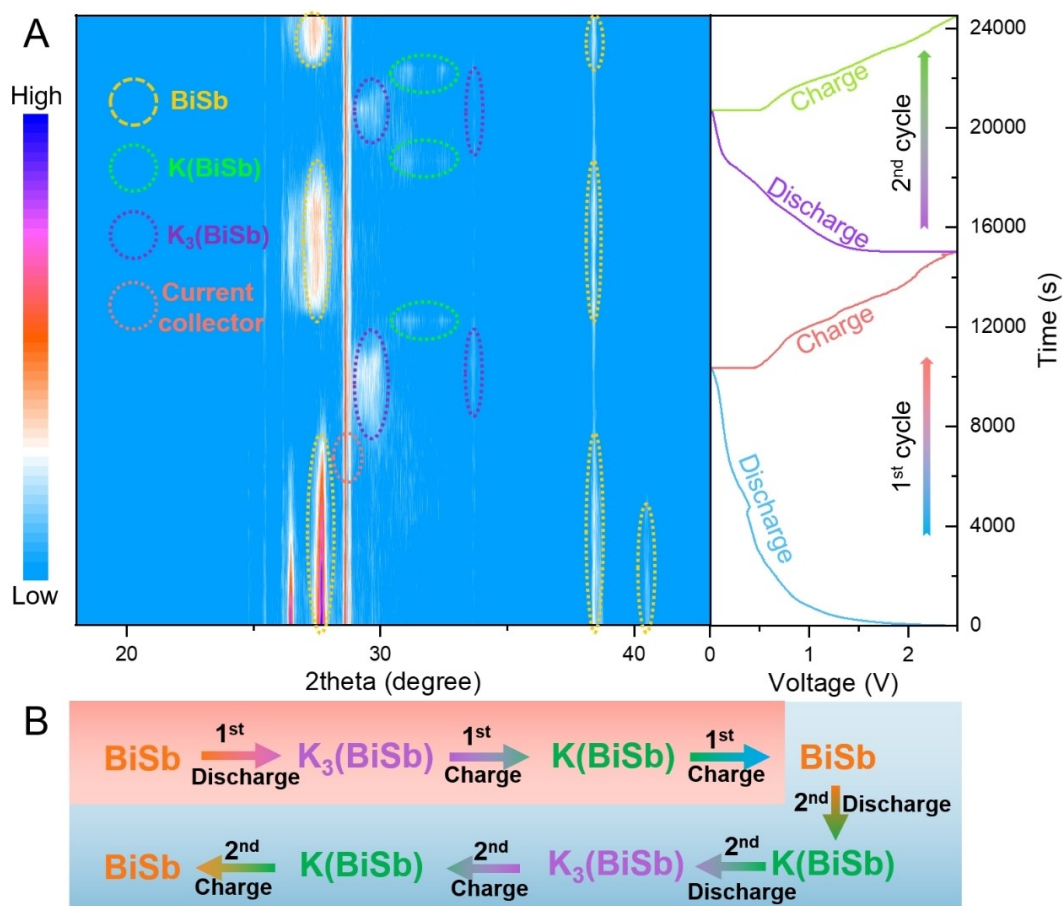


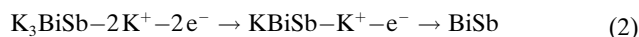
Figure 5. A) Contour plot of the in situ XRD patterns of BiSb-HTR anode and the corresponding charge/discharge curve during the 1st and 2nd K⁺ insertion/extraction cycles. B) Schematic illustration of the potassium storage mechanism.

are different. These phenomena demonstrate the high reversibility of the BiSb-HTR anode during potassiation/depotassiation processes (Figure 5B). The relevant electrochemical reactions can be summarized as follows:

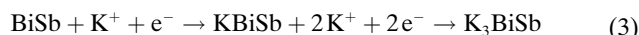
1st discharge process:



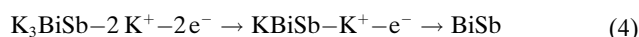
1st charge process:



2nd discharge process:



2nd charge process:



To investigate the origin of the superb potassium storage property of the BiSb-HTR electrode, the galvanostatic intermittent titration technique (GITT) test and capacitive-effect contribution calculation were carried out. The two electrodes are charged in the first cycle by applying a pulse current at 0.05 A g^{-1} for a duration period of 20 min and relaxation intervals for 2 h (Figure S11A). Figure S11B shows the K-ion diffusion coefficients of two anodes from GITT curves. Noticeably, a higher K^+ diffusivity coefficient in the BiSb-HTR anode is observed compared with that in the BiSb-TFA anode during the potassiation/depotassiation process. These results manifest that the ultrafine particle size ($\approx 15 \text{ nm}$) of the BiSb-HTR contributes to the fast

diffusion of K ions, accounting for the enhanced electrochemical kinetics and the preminent cycling performance.^[24]

To further investigate the composition and morphology evolution of the BiSb-HTR anode, ex situ TEM and SEM were conducted and results are shown in Figure S12. The inset of Figure S12A presents the digital photograph of the BiSb-HTR electrode after 1000 cycles. It is seen that the electrode is intact (i.e., the active material does not fall off from the Cu foil), signifying that the BiSb-HTR anode can effectively relieve the stress/strain arising from the volume fluctuation during repeated charge/discharge processes. As shown in Figure S12A, the uniform distribution of the ultrasmall nanoparticles is well maintained after battery cycling, without noticeable particle agglomeration. The HRTEM image in Figure S12B contains featured lattice spacing of 0.32 nm for the (012) plane of BiSb alloy, indicating the preserved crystallinity of the anode material. The EDX-elemental mapping images reveal the homogeneous distribution of Bi, Sb and K after cycling (Figure S12C and S12D), which is agreeing well with the original images for the freshly prepared BiSb-HTR.

The potassium-ion full battery was assembled using a PTCDA cathode and a BiSb-HTR anode, as depicted in Figure 6A. Before the study on full battery, the electrochemical properties of the PTCDA cathode are tested in half-cells using metallic potassium as counter electrode. The test results demonstrate a reversible specific capacity of 134.0 mAh g^{-1} after 50 cycles at 0.1 A g^{-1} and good cycling durability in a voltage range of $1.5\text{--}3.5 \text{ V}$ (Figure S13). As presented in Figure S14A, the working voltage interval of the BiSb-HTR/PTCDA full cell is set over $0.8\text{--}3.2 \text{ V}$. Figure 6B and C show that the BiSb-HTR/PTCDA battery

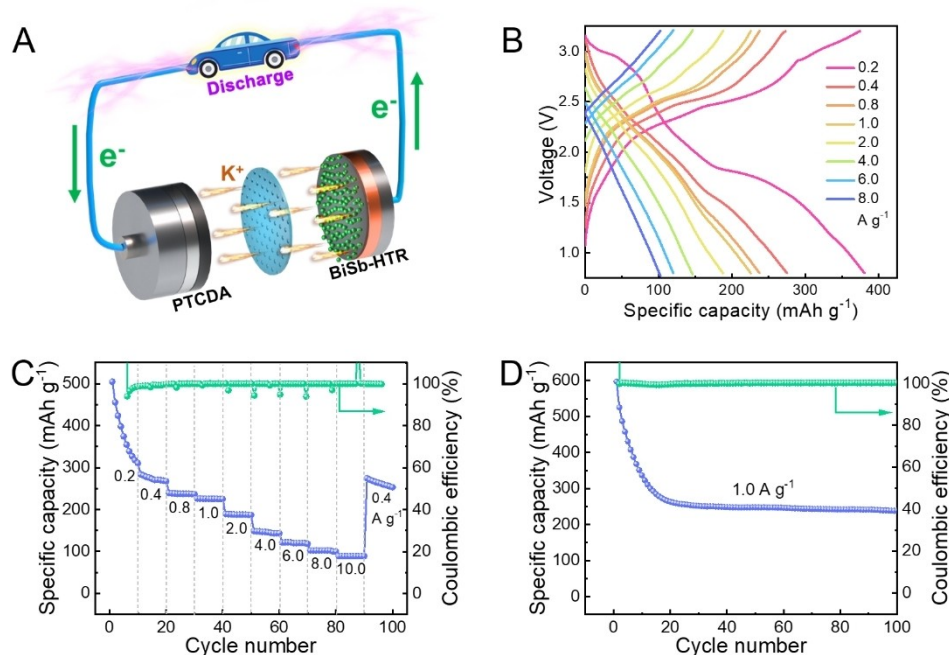


Figure 6. A) Schematic illustration of the discharge mechanism of BiSb-HTR//PTCDA K-ion full cell. Electrochemical performance of BiSb-HTR//PTCDA full cell: B) Charge/discharge curves and C) rate capability at different current densities. D) Cycling performance at 1.0 A g^{-1} .

achieves competitive specific capacities of 380.6, 275.0, 237.6, 225.6, 187.8, 146.6, 120.0, 102.3 and 88.9 mAhg⁻¹ (calculated based on anode mass) at various current rates from 0.2 to 10.0 Ag⁻¹. Additionally, the full cell exhibits a good cycling performance, where a reversible specific capacity of 238.4 mAhg⁻¹ (calculated based on the anode mass) and a high CE of 100% after 100 cycles at 1.0 Ag⁻¹ is maintained (Figure 6D). The capacity loss in the initial cycles of the BiSb-HTR/PTCDA K-ion full cell is related to the formation of SEI film on BiSb-HTR anode,^[21] which is actually consistent with the initial cycling performance of BiSb-HTR anode in half-cells. The capacity loss is also a common observation in previously reported work^[6a] due to the formation of SEI film. As shown in Figure S14B, the

assembled full cell can successfully light up a lamp set with three light-emitting diodes (LED) bulbs, demonstrating the practical application prospect of BiSb-HTR anode in advanced KIBs.

More importantly, the rapid HTR synthetic method based on radiative heating is not only limited to the specific BiSb alloy above but also can be readily extended to the manufacture of other bimetallic alloy nanoparticles, which creates more opportunities for the applications of nano-sized high-quality alloys (Figure 7A). To validate the universality and versatility of this HTR technique, we successfully synthesized other high-quality bimetallic alloy nanoparticles, such as SnSb, CoSb, NiSb, FeSb, SnBi, and Cu₂Sb, from the corresponding precursor powders (Figure S15). XRD pat-

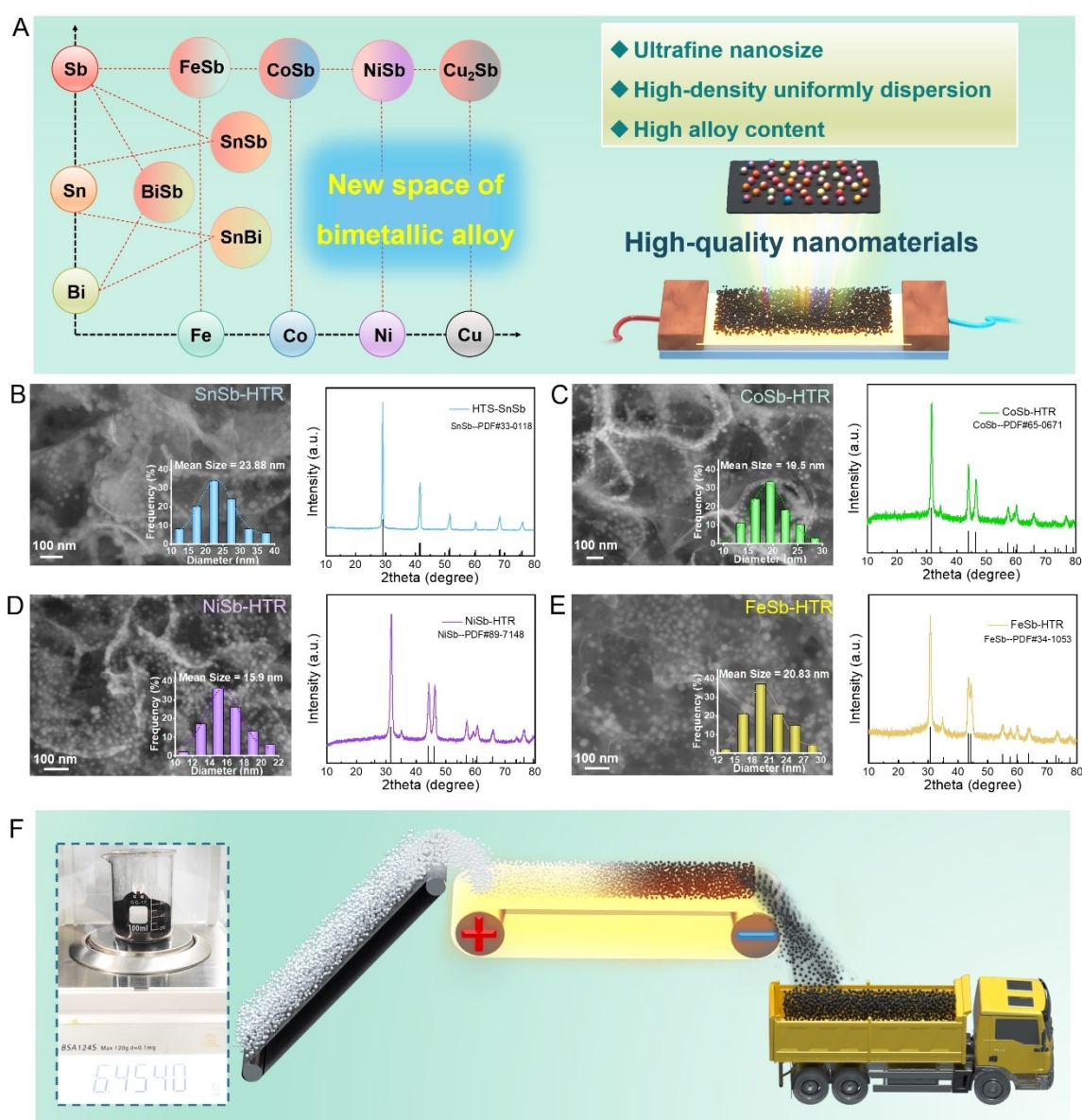


Figure 7. A) The compositional designs in a neural network diagram. Extended new space of bimetallic alloy by our HTR method. Schematic illustration of the combinatorial synthesis of an extensive series of high-quality bimetallic alloy nanoparticles. B)–E) High magnification SEM images, nanoparticle size distributions, XRD patterns, and TGA curves of SnSb, CoSb, NiSb, and FeSb. F) Schematic illustration of the roll-based large-scale production of high-quality anode nanomaterials.

terns of the HTR-fabricated binary nanocomposites can match well with the corresponding standard cards, corroborating the successful transition of the precursor into bimetallic alloy nanoparticles after the present ultrafast HTR treatment. Figure 7B–E, Figures S16 and S17 show the SEM images of the SnSb, CoSb, NiSb, FeSb, Cu₂Sb and SnBi samples at different magnifications, where numerous nanoparticles are homogeneously distributed on carbon matrix with average particle sizes of 23.9 nm for SnSb, 19.5 nm for CoSb, 15.9 nm for NiSb, 20.8 nm for FeSb, 19.0 nm for Cu₂Sb and 20.6 nm for SnBi. Besides, according to the TGA results in Figure S18, the alloy contents of the SnSb, CoSb, NiSb, FeSb, Cu₂Sb and SnBi nanocomposites manufactured through the HTR treatment are maintained at a higher level, which is extremely important for the practical application of alkali metal ion batteries. Based on the high practicability and efficiency of this HTR synthetic technique, we were able to produce over 6.4 g of the BiSb nanomaterials (Inset of Figure 7F). This ability to synthesize a broad range of high-quality bimetallic nanoparticles reveals the universality of our high-effective and facile strategy for manufacturing high-performance KIBs anodes. Such universality, predictably, can lead to high-efficient, lost-cost and large-scale manufacturing of high-quality anode materials for EESSs, when combined with the well-developed roll-to-roll system (Figure 7F).

Conclusion

In summary, we develop an ultrafast and general HTR method for the fabrication of high-quality bimetallic alloy nanocomposites. The unique features (i.e., ultrahigh ramping/cooling rates and seconds-short heating durations) of the HTR process ensure the synthesis of ultrafine bimetallic alloy nanoparticles with narrow size distribution, uniform dispersion, and high metal content, which correspondingly contribute to surpassing the inherent limitations of traditional TFA synthesis method. As a proof-of-concept demonstration, we utilize the HTR strategy in the rapid synthesis of high-quality BiSb nanoparticles. The obtained BiSb-HTR can be used as a promising anode for KIBs, delivering ultrahigh cycling stability over 800 cycles (0.0088 % decay rate with the remaining capacity of 324.8 mAh g⁻¹) than those of the KIBs based on the Sb-HTR and BiSb-TFA anodes. The electrochemical reaction mechanism of BiSb ↔ KBiSb ↔ K₃BiSb during the charge/discharge process is proved by in situ XRD. Additionally, the HTR synthetic technique is extendable to prepare other bimetallic alloy nanoparticles, such as SnSb, CoSb, NiSb, FeSb, SnBi, and Cu₂Sb, indicating universality and versatility. This work can pave a new path for the ultrafast nanomanufacturing of high-performance alloying anode, which is currently hard to be achieved by conventional methods.

Acknowledgements

This work was financially supported by the fundamental research fund from Shenzhen (JCYJ20220531095214032), Shenzhen Science and Technology Program (Grant No. ZDSYS20190902093220279), and National Natural Science Foundation of China (Grant Nos. 52171219, 91963113).

Conflict of Interest

The authors declare no conflict of interest.

Data Availability Statement

The data that support the findings of this study are available from the corresponding author upon reasonable request.

Keywords: Bimetallic Alloy · High-Temperature Radiation · In Situ X-Ray Diffraction · Nanomanufacturing · Potassium-Ion Batteries

- [1] S. Imtiaz, I. S. Amiin, Y. Xu, T. Kennedy, C. Blackman, K. M. Ryan, *Mater. Today* **2021**, *48*, 241–269.
- [2] X. Min, J. Xiao, M. Fang, W. Wang, Y. Zhao, Y. Liu, A. M. Abdelkader, K. Xi, R. V. Kumar, Z. Huang, *Energy Environ. Sci.* **2021**, *14*, 2186–2243.
- [3] a) L. Wang, B. Zhang, B. Wang, S. Zeng, M. Zhao, X. Sun, Y. Zhai, L. Xu, *Angew. Chem. Int. Ed.* **2021**, *60*, 15381–15389; b) H. Huang, J. Wang, X. Yang, R. Hu, J. Liu, L. Zhang, M. Zhu, *Angew. Chem. Int. Ed.* **2020**, *59*, 14504–14510; c) F. Xie, L. Zhang, B. Chen, D. Chao, Q. Gu, B. Johannessen, M. Jaroniec, S.-Z. Qiao, *Matter* **2019**, *1*, 1681–1693.
- [4] K. Song, C. Liu, L. Mi, S. Chou, W. Chen, C. Shen, *Small* **2021**, *17*, 1903194.
- [5] P. Xiong, J. Wu, M. Zhou, Y. Xu, *ACS Nano* **2020**, *14*, 1018–1026.
- [6] a) C. Huang, A. Xu, G. Li, H. Sun, S. Wu, Z. Xu, Y. Yan, *Small* **2021**, *17*, 2100685; b) V. Gabaudan, R. Berthelot, M. T. Sougrati, P.-E. Lippens, L. Monconduit, L. Stievano, *J. Mater. Chem. A* **2019**, *7*, 15262–15270; c) J. Han, K. Zhu, P. Liu, Y. Si, Y. Chai, L. Jiao, *J. Mater. Chem. A* **2019**, *7*, 25268–25273; d) Z. Li, Q. Gan, Y. Zhang, J. Hu, P. Liu, C. Xu, X. Wu, Y. Ge, F. Wang, Q. Yao, Z. Lu, J. Deng, *Nano Res.* **2022**, *15*, 217–224.
- [7] a) Q. Dong, M. Hong, J. Gao, T. Li, M. Cui, S. Li, H. Qiao, A. H. Brozena, Y. Yao, X. Wang, G. Chen, J. Luo, L. Hu, *Small* **2022**, *18*, 2104761; b) P.-C. Chen, X. Liu, J. L. Hedrick, Z. Xie, S. Wang, Q.-Y. Lin, M. C. Hersam, V. P. Dravid, C. A. Mirkin, *Science* **2016**, *352*, 1565–1569.
- [8] a) M. Cui, C. Yang, S. Hwang, B. Li, Q. Dong, M. Wu, H. Xie, X. Wang, G. Wang, L. Hu, *Nano Lett.* **2022**, *22*, 255–262; b) M. Guo, Q. Dong, H. Xie, C. Wang, Y. Zhao, X. Wang, W. Zhong, Z. Li, R. Wang, Y. Wang, L. Hao, S. He, G. Chen, W. Xiong, J.-C. Zhao, L. Hu, *Matter* **2022**, *5*, 594–604; c) M. Cui, C. Yang, S. Hwang, M. Yang, S. Overa, Q. Dong, Y. Yao, A. H. Brozena, D. A. Cullen, M. Chi, T. F. Blum, D. Morris, Z. Finckel, X. Wang, P. Zhang, V. G. Goncharov, X. Guo, J. Luo, Y. Mo, F. Jiao, L. Hu, *Sci. Adv.* **2022**, *8*, abm4322.
- [9] S. Dou, J. Xu, X. Cui, W. Liu, Z. Zhang, Y. Deng, W. Hu, Y. Chen, *Adv. Energy Mater.* **2020**, *10*, 2001331.

- [10] Y. Yao, Z. Huang, P. Xie, S. D. Lacey, R. J. Jacob, H. Xie, F. Chen, A. Nie, T. Pu, M. Rehwoldt, *Science* **2018**, 359, 1489–1494.
- [11] Z. Huang, Y. Yao, Z. Pang, Y. Yuan, T. Li, K. He, X. Hu, J. Cheng, W. Yao, Y. Liu, A. Nie, S. Sharifi-Asl, M. Cheng, B. Song, K. Amine, J. Lu, T. Li, L. Hu, R. Shahbazian-Yassar, *Nat. Commun.* **2020**, 11, 6373.
- [12] Q. Wu, B. Chen, H. Xie, X. Bai, M. Liang, Z. Wu, X. Jin, C. He, N. Zhao, *Chem. Eng. J.* **2022**, 430, 132906.
- [13] a) Z. Wang, C. Duan, D. Wang, K. Dong, S. Luo, Y. Liu, Q. Wang, Y. Zhang, A. Hao, *J. Colloid Interface Sci.* **2020**, 580, 429–438; b) K.-T. Chen, Y.-C. Yang, L.-M. Lyu, M.-Y. Lu, H.-Y. Tuan, *Nano Energy* **2021**, 88, 106233; c) X.-D. He, J.-Y. Liao, S. Wang, J.-R. Wang, Z.-H. Liu, X. Ding, Q. Hu, Z.-Y. Wen, C.-H. Chen, *J. Mater. Chem. A* **2019**, 7, 27041–27047; d) K.-T. Chen, H.-Y. Tuan, *ACS Nano* **2020**, 14, 11648–11661; e) J. Qin, T. Wang, D. Liu, E. Liu, N. Zhao, C. Shi, F. He, L. Ma, C. He, *Adv. Mater.* **2018**, 30, 1704670.
- [14] S. Dou, J. Xu, C. Yang, W.-D. Liu, I. Manke, W. Zhou, X. Peng, C. Sun, K. Zhao, Z. Yan, Y. Xu, Q. Yuan, Y. Chen, R. Chen, *Nano Energy* **2022**, 93, 106903.
- [15] Y. Liang, N. Song, Z. Zhang, W. Chen, J. Feng, B. Xi, S. Xiong, *Adv. Mater.* **2022**, 34, 2202673.
- [16] W. Zhang, J. Yin, M. Sun, W. Wang, C. Chen, M. Altunkaya, A.-H. Emwas, Y. Han, U. Schwingenschlogl, H. N. Alshareef, *Adv. Mater.* **2020**, 32, 2000732.
- [17] F. Xu, Y. Zhai, E. Zhang, Q. Liu, G. Jiang, X. Xu, Y. Qiu, X. Liu, H. Wang, S. Kaskel, *Angew. Chem. Int. Ed.* **2020**, 59, 19460–19467.
- [18] Y. Yamada, J. Wang, S. Ko, E. Watanabe, A. Yamada, *Nat. Energy* **2019**, 4, 269–280.
- [19] N. Chen, N. Shen, X. Yi, Y. Pang, J. Zheng, Q. Lai, Y. Liang, *J. Energy Chem.* **2023**, 76, 51–58.
- [20] X. Liu, X. Yu, Y. Tong, Y. Sun, W. Mai, L. Niu, H. Li, *Chem. Eng. J.* **2022**, 446, 137329.
- [21] L. Zhou, Z. Cao, J. Zhang, H. Cheng, G. Liu, G.-T. Park, L. Cavallo, L. Wang, H. N. Alshareef, Y.-K. Sun, J. Ming, *Adv. Mater.* **2021**, 33, 2005993.
- [22] a) C.-H. Chang, K.-T. Chen, Y.-Y. Hsieh, C.-B. Chang, H.-Y. Tuan, *ACS Nano* **2022**, 16, 1486–1501; b) Z. Sun, Y. Liu, W. Ye, J. Zhang, Y. Wang, Y. Lin, L. Hou, M.-S. Wang, C. Yuan, *Angew. Chem. Int. Ed.* **2021**, 60, 7180–7187.
- [23] a) Z. Wang, K. Dong, D. Wang, S. Luo, Y. Liu, Q. Wang, Y. Zhang, A. Hao, C. Shi, N. Zhao, *J. Mater. Chem. A* **2019**, 7, 14309–14318; b) Y. Yang, J. Wang, S. Liu, W. Zhu, G. Ye, X. Yi, B. Lu, *Chem. Eng. J.* **2022**, 435, 134746; c) X. Xiang, D. Liu, X. Zhu, K. Fang, K. Zhou, H. Tang, Z. Xie, J. Li, H. Zheng, D. Qu, *Appl. Surf. Sci.* **2020**, 514, 145947; d) Q. Liu, L. Fan, R. Ma, S. Chen, X. Yu, H. Yang, Y. Xie, X. Han, B. Lu, *Chem. Commun.* **2018**, 54, 11773–11776; e) Z. Yi, N. Lin, W. Zhang, W. Wang, Y. Zhu, Y. Qian, *Nanoscale* **2018**, 10, 13236–13241; f) B. Wang, Z. Deng, Y. Xia, J. Hu, H. Li, H. Wu, Q. Zhang, Y. Zhang, H. Liu, S. Dou, *Adv. Energy Mater.* **2020**, 10, 1903119.
- [24] X. Ge, S. Liu, M. Qiao, Y. Du, Y. Li, J. Bao, X. Zhou, *Angew. Chem. Int. Ed.* **2019**, 58, 14578–14583.

Manuscript received: March 10, 2023

Accepted manuscript online: April 11, 2023

Version of record online: May 12, 2023